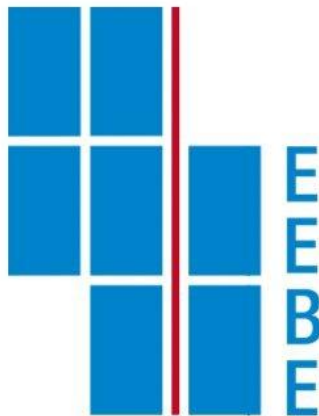FINAL DEGREE PROJECT

Biomedical Engineering Degree

SIMULATION OF LEFT-RIGHT ASYMMETRY IN HEART MORPHOGENESIS

Report and Annexes

Author: Ignacio Pérez Meroño

Director: Jose Javier Muñoz Romero

Tutor: Cristina Corral Ortega (UPV)

Summons: June, 2022

INDEX

SUMMARY/ABSTRACT

There are several studies on the heart morphogenesis in the vertebrate embryo, and in particular on how during the development of the heart tube bilateral symmetry is broken leading to morphogenesis with left-right asymmetry. Despite clinical and experimental findings, it is still not entirely clear how left-right patterning drives asymmetric morphogenesis, as the focus has generally been on a simple description of the direction of the loop. One way to overcome the conundrums in clinical research is to use predictive computational models to help explore shape variations during heart development, depending on the congenital anomaly to be studied. Heterotaxy, as a set of pathologies affecting the spatial structure of the heart due to left-right asymmetry (among others), can lead to cardiovascular diseases, so it is of particular relevance to find the origin of this anomaly and the different configurations that can lead to its emergence. One of them is known as "Transposition of the great arteries (TGA)" and is suspected to be due to a twist of the outflow tract (OFT) during morphogenesis. For this study we aimed to predict, through computational simulations and using discretization and finite element meshing methods, the morphogenesis of a heart model developed after the heart tube loop when the OFT region does not grow, mainly using the quantification of the twist angle. The results provide an insight into the mechanism of the cardiac loop, where the flipping tendency is to the right leading to a re-organization of the ventricles as the first finding. This is relevant for congenital heart defects as well as for the estimation of the left-right pattern in the morphogenesis of the heart in order to get a better classification in the different classes of heterotaxy syndrome.

ACKNOWLEDGEMENTS

I would like to thank all the people who have made this work possible. My sincere thanks go to my tutor Jose Javier Muñoz Romero, for his support, patience, and always accurate guidance.

In a similar vein, I would like to thank all those that accompanied me throughout the development of this project. The motivation and enthusiasm they have fostered have been immeasurable.

Furthermore, I would like to express my gratitude to the Polytechnic University of Catalonia and the Polytechnic University of Valencia for allowing me to conduct this research, especially to the LaCàn research group for providing me with the support and the necessary tools for the elaboration of the project.

And finally, thanks to Sigolene Meilhac and Segolene Bernheim, from Image Institute - Institut Pasteur (Paris, France) for providing the data of the heart geometry.

GLOSSARY

Buckling: A mechanical instability, characterized by a sudden sideways deformation. It applies to the growth of the heart tube, when constrained between fixed poles, and thus undergoes looping as a result of buckling (also see Fig. 2).

Cardiomyocytes: Cardiac muscular cells that are capable of spontaneously and individually contracting. They are also specialized in excitation and conduction of action potentials.

Cell-fate mapping: This method is used by developmental biologists to determine which tissues and structures are embryonic in origin. Each cell type or group of cells is assigned a fate in the embryo, indicating which parts of the embryo will develop into which tissues. This process is called cell lineage tracing when it is carried out at a single-cell resolution. It is also used to track tumours' growth.

Chirality: From the Greek 'hand', describes the asymmetric property of objects, such as the hand, which cannot be superimposed on their mirror image.

Convergence-extension: The process by which cells within a tissue converge along one axis and extend along a perpendicular axis. This process drives tissue deformation during organogenesis, with a combined narrowing on one axis and elongation perpendicularly.

Dorsal mesocardium: A dorsal tissue in amniotes, which initially attaches the heart tube to the dorsal pericardial wall, beneath the foregut. It is progressively broken during heart looping, corresponding to dorsal closure of the heart tube.

Situs: Based on the term 'position' in Latin, this term describes whether an organ or segment of the heart is normal (situs solus), mirror-imaged (situs inversus) or incoherent (situs ambiguous or heterotaxy).

PREFACE

1.1 Background

Cardiovascular diseases are a major cause of medical care, hospital admissions, disability and other health consequences. According to data provided by the World Health Organization (WHO, 2022), cardiovascular diseases are the leading cause of death and disability in the world, killing 17.5 million people each year. A large proportion of these deaths are due to a group of syndromes known as heterotaxy. The heterotaxy syndromes are a class of diseases in which cardiac structures are misaligned with one another or with other organs, resulting in a number of congenital heart conditions. This results in a plethora of congenital heart diseases, including alterations of the visceral situs (Carro Hevia et al., 2011).

1.2 Motivation

One of the major significances of this type of cardiac anomaly resulting from heterotaxy is the high prevalence of congenital heart disease, many of which have a complex outcome, and extracardiac pathologies related to other surrounding organs. It is essential to know the origin and causes of a particular disease, as well as to determine its possible effects in a preventive manner, in order to understand it. However, the use of only experimental methods is not always the best approach to finding a solution. In situations where animal experiments are too slow, computational simulations offer scientific value, economic value, and ethical value. Therefore, this relatively easy-to-implement technology is enabling the medical and health sectors to benefit from technological advancements promoted by computational simulation.

1.3 Previous requirements

In order to create the work, it has been necessary to have the data of the model to which the preprocessing, processing, and development of the various models executed were subsequently applied. This information is being provided by a researcher affiliated with the Pasteur Institute in Paris, who has requested collaboration from the UPC to prepare the study, which is part of a previously initiated research paper. Furthermore, it was necessary to have a cluster at the Department of Applied Mathematics III at the UPC since the simulations took too much time for their correct execution and convergence, specifically from the LaCan group, a HPC Beowulf cluster with 33 compute nodes (1 acquired in 2013, 3 acquired in 2015, 2 acquired in 2016, 20 acquired in 2018 and 7 acquired in 2020), one master node and one storage node. All nodes are connected using an Infiniband network.

INTRODUCTION

<u>Heart morphogenesis</u>

In vertebrates, the heart is the first organ to form, and has a vital role in the distribution of nutrients and oxygen in the embryo. Initially it functions as a cardiac tube and is principally composed of a contractile myocardium that is essential for its action as a central pump. Subsequently, regionalization of this structure takes place, and in adult birds and mammals this leads to the formation of the four-chambered heart (Buckingham et al., 2005). This organ is an asymmetric organ. Particularly, in humans it is positioned on the left side of the thoracic cavity. In addition, it is partitioned in two halves, driving a double blood circulation. The atrial and ventricular chambers, as well as the great vessels, in the left and right halves of the heart have distinct anatomical features, which are adapted to the systemic and pulmonary circulation, respectively (Desgrange et al., 2018).

Through cell-fate mapping studies, histological sectioning, and 3D reconstructions, animal models have provided a wealth of biological information on the earliest structures of the developing heart (Ivanovitch et al., 2017). Given the ethical concerns associated with studying human embryos, we do not have a lot of data on human development to compare to animal models. It is therefore vital to construct human models of heart development that can allow for the examination of innate cellular behavior and its effect on cardiac morphogenesis and function. Researchers are proposing to use stem cell-derived cardiac cell populations with modern tissue engineering approaches to develop models of the earliest structure in the sequence of embryonic cardiac development, namely, the linear cardiac tube (Mandrycky et al., 2020).

The primitive heart tube is one of the earliest structures to form in the human embryo just 3 weeks after fertilization. It is highly conserved among vertebrates that the rightward bend or loop of the heart tube is the first event that breaks developmental symmetry. For the correct alignment of cardiac chambers and thus for the establishment of the double blood circulation, this looping of the heart is required. Having left-right patterning in humans is associated with a wide range of conditions known as heterotaxy, with an incidence of about 1/10000, including defects in the lung, spleen, liver, stomach, intestine and also complex cardiac malformations, which will determine patient outcome (Lin et al., 2014; Guimier et al., 2015). For example, in Nodal mutants (Brennan et al., 2002), the direction of the cardiac loop is randomized, but the looping process still occurs. Researchers Brown and Wolpert (1990) hypothesized the existence of an additional, organ-specific mechanism to generate the asymmetry in growth in a random fashion. However, the basis of such a mechanism for loop formation in the heart tube remains enigmatic (Le Garrec et al., 2017).

Tube Looping formation

● State of the art

First, a linear heart tube is composed of two layers of dormant heart cells (cardiomyocytes) surrounding a layer of cardiac jelly, which keeps the cardiomyocytes from coming into contact with a layer of endocardial cells lining the hollow lumen (Männer et al., 2019; Sizarov et al., 2011). Researchers found that certain regions of the linear heart tube are destined to become the atrial and ventricular chambers of the adult heart (Fig. 1A) (Van Vliet et al., 2012). Shortly after the linear heart tube forms, it begins to increase in size and rotate, or loop, by intrinsic and extrinsic mechanisms to the right side to create a C-shaped curve (C-shaped heart tube). As a result, the section of the heart tube that becomes the ventricles relocates downward, forming the S-shaped heart tube. During the final stage of the loop, the aorta nestles between the developing atria to form a four-chambered organ.
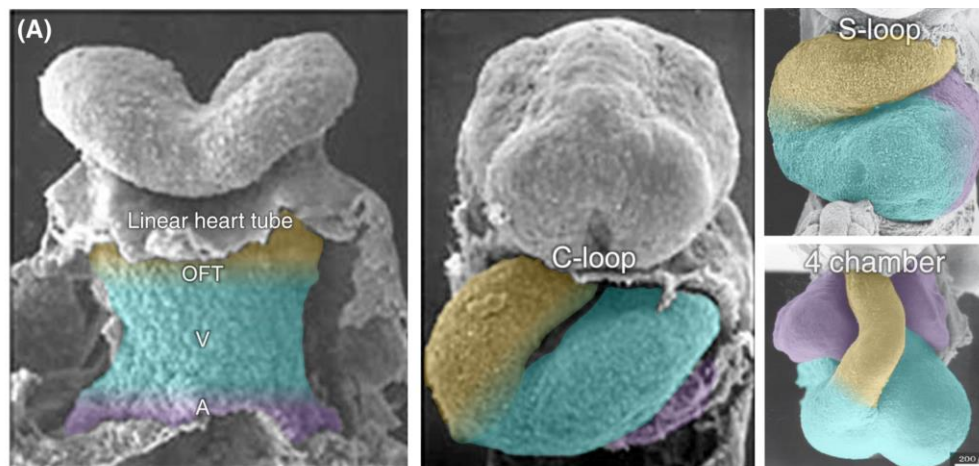
Figure 1.(A) SEM images of the developing human heart tube from a linear heart tube, C-looped, S-looped, and four-chambered heart (4 ch). Future outflow tracts (OFT; yellow), ventricles (V; blue), and atria (A; purple) are color coded to highlight the complex structural transition that the heart tube undergoes during morphogenesis. Color coding is a rough anatomical estimation and not exact (Oostra et al., 2007).

● Intrinsic and extrinsic mechanisms

In the context of the deformation of tubular organs, intrinsic mechanisms are determined by the interaction between cells within the tube, while extrinsic mechanisms are determined by the external forces acting on the tube, such as those at the tube's edges or those resulting from embryonic processes external to the tube.

For intrinsic mechanisms, we consider growth rate and orientation. Rate may be the result of cell proliferation or growth, while orientation implies that cells can perceive a reference axis, at a

tissue or embryonic level, so that the tissue becomes polarized and the cells behave accordingly. One of the best ways to assess these parameters outside the animal model environment is through computational simulations. With these it is possible to define a pattern of growth zones (with a higher growth rate, but a constant orientation, and vice versa) capable of generating the tube loop. These models provide an indication of how intrinsic mechanisms might contribute to the formation of tube loops, yet these mechanisms must be confirmed experimentally based on correct morphogenesis of isolated tubes.

There can also be extrinsic mechanisms that lead to tube loop formation, as in chick intestinal rotation, where the dorsal mesentery shows left-right asymmetry in its cellular architecture, which is dictated by left Nodal/Pitx2 determinants. Consequently, the dorsal mesentery tilts, exerting forces on the intestinal tube attached to it (Davis et al., 2008). It is also possible that other extrinsic mechanisms are involved, such as convergence-extension (Chen et al., 1998; Iwaki and Lengyel, 2002; Karner et al., 2009; Wang et al., 2005), or buckling, a concept proposed over a century ago that illustrates, when the heart tube grows longitudinally with a fixed distance between its poles, the tube is deformed.

Both intrinsic and extrinsic mechanisms show that the geometry of the growth patterns is crucial to determining whether the final tube adopts a helical or S-shaped shape. The tube will deform in 2D if the growth patterns are within the same plane along the tube axis (Fig. 2Aii, Bii, Cii). In contrast, a helical shape requires breaking this flat configuration. There are different methods for achieving this: by introducing a third differential growth zone (Fig. 2Ai), by establishing a 120° separation on the circumference between the zones that define the orientation bias (Fig. 2Bi) or by introducing asymmetries that influence buckling (Fig. 2Ci).

Generally, these types of computer simulations point to potential mechanisms that could explain a heart-specific random generator of asymmetry, as described by Brown and Wolpert (1990), researchers mentioned above. Furthermore, intrinsic and extrinsic mechanisms are not mutually exclusive and can operate in concert to generate morphogenesis. There have however been explant studies that have shown that isolated cardiac tubes do have a curvature (Manning and McLachlan, 1990), indicating that intrinsic rather than extrinsic factors are responsible for cardiac loop formation. The explants generated a C-shaped tube, but not a helical shape. Additionally, surgical disconnection of only one pole (the arterial pole) impaired cardiac looping (Kidokoro et al., 2008). Thus, the role of intrinsic and extrinsic factors in the cardiac loop remains unclear and the basis of such a mech-anism for the looping of the heart tube remains relatively unintelligible.
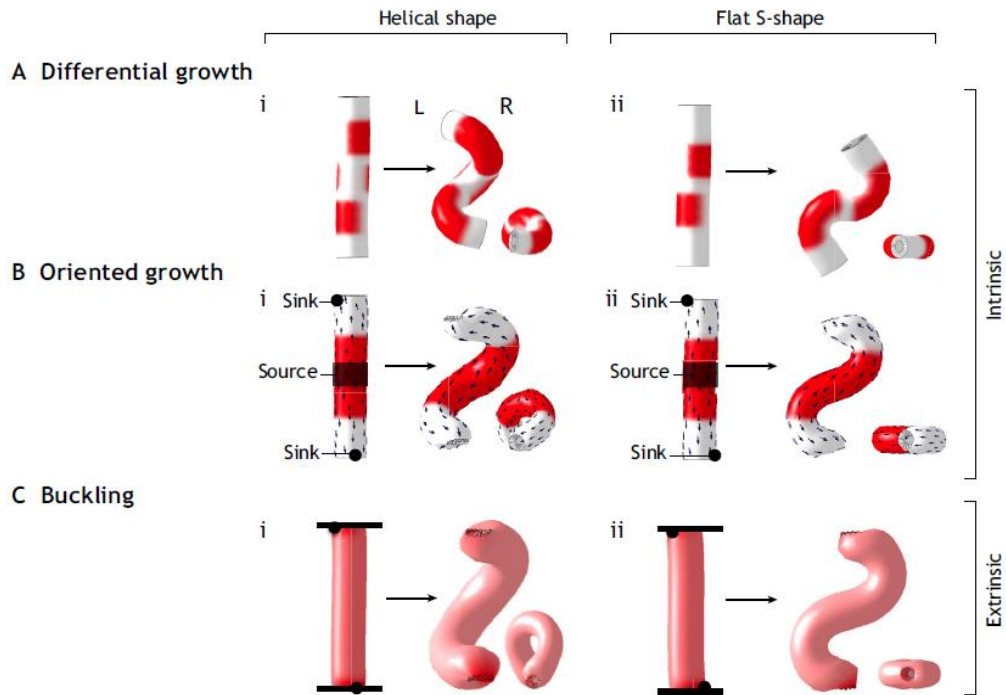
Figure 2. Theoretical intrinsic and extrinsic mechanisms of tube looping. Simulations of tube looping with a finite element model (described by Le Garrec et al.,2017). Three looping mechanisms (differential growth, oriented growth or buckling; A-C). (A) Differential growth within the heart tube. Higher (dark red) longitudinal growth (i.e. along the tube axis) can be generated in three bands positioned along the tube length in a helical configuration (right in the upper band, ventral in the middle band, left in the lower band). Two bands of higher longitudinal growth can be generated on either side (left/right) of the tube to create a flat-S shape (Aii). (B) Oriented growth within the heart tube. Simulations assume uniform growth rates in a large band (red). The direction of growth is determined by a morphogen, synthesized at a central source and degraded in two sinks, at each pole of the tube (black arrows). In the 3D setting (Bi), the sinks are positioned at 120° relative to each other, leading to a helical shape. In the 2D setting (Bii), the sinks are positioned on each side of the tube, leading to a flat-S shape. (C) Buckling, as an example of an extrinsic mechanism. In contrast to the previous simulations, the two poles of the tube are fixed in all three directions (black bars). All along the tube, growth is uniform except at the poles, where growth is higher. The 3D setting (Ci) positions regions of high growth at 120° relative to each other, producing a helix. In 2D mode (Cii), regions with high growth are positioned on either side (left/right) of the tube, resulting in a flat S.

Theoretical basis of the computational models

To carry out the experimental problems and the changes of the mechanical behaviour of the tissue through computational simulations it is crucial to employ fractional viscoelastic models and magnetic resonance imaging, together to develop the behaviour of the tissue, the heart in our case. Accordingly, basic potential functions (W) and force contributions (g) are established for this type of problem, leading to a rapid derivation of expressions for implementation in finite element models (Bonet and Wood, 1997). It should be borne in mind that this part has already been developed by research at the Pasteur® Institute, so we start from a meshed model to which we will then apply the viscoelasticity formulae computationally, as well as the boundary conditions. We next describe briefly the main aspect of the computational model:

Viscoelasticity

We assume a decomposition of the total displacements u into an elastic component $\boldsymbol{u}^e$ and a viscous component $\boldsymbol{u}^v$ ($\boldsymbol{u} = \boldsymbol{u}^e + \boldsymbol{u}^v$), as well as a multiplicative decomposition of the deformation gradient $\boldsymbol{F} = \boldsymbol{F}_v \cdot \boldsymbol{F}_e$. According to a Maxwell model, we will assume a stress value common to the viscous and elastic part:

$$S = \frac{\partial W(\boldsymbol{E}^e)}{\partial \boldsymbol{E}^e} = \eta \boldsymbol{E}^v \tag{1}$$

The integral of this equation will allow the viscous deformation to be calculated from the elastic deformation $\boldsymbol{E}_e$ (or the total, since $\boldsymbol{F}_e = (\boldsymbol{F}_v) - 1$). The elastic deformation can be obtained by minimizing the elastic energy (or mechanical equilibrium):

$$\delta W(\boldsymbol{E}^e) = \int_\Omega \boldsymbol{S} : \delta \boldsymbol{E}^e dV = \delta \boldsymbol{x}^a \cdot \boldsymbol{g}^a \tag{2}$$

Adding Growth

A multiplicative decomposition of the deformation gradient is used to add growth to the model:

$$\boldsymbol{F} = \boldsymbol{F}_e \cdot \boldsymbol{F}_g \tag{3}$$

The stresses are due to the elastic component $\boldsymbol{F}_e$ only, i.e. $\boldsymbol{E}_e = \frac{1}{2}(\boldsymbol{F}_e^T \boldsymbol{F}_e)$, with $\boldsymbol{F}_e = \boldsymbol{F} \boldsymbol{F}_g^{-1}$. The stress in the intermediate configuration is given by:

$$S_e = J_e \boldsymbol{F}_e^{-1} \sigma \boldsymbol{F}_e^{-T} \tag{4}$$

For computing the residual, the elastic energy is solely dependent on the elastic component $W(\boldsymbol{E}^E)$. This is conjugated to the nodal positions $\boldsymbol{x}^a$, resulting in the expression:

$$\boldsymbol{g}^e = \int_{\Omega^e} \frac{\delta w(\boldsymbol{E}_e)}{\delta \boldsymbol{F}_e} \boldsymbol{F}_g^{-T} \nabla N^a dV \tag{5}$$

Contact setting

There are a multitude of prototypes to be simulated in which contact influences the final result and which must therefore be taken into account when setting the parameters of the model. A quick manner to simulate contact problems is by adding a contact potential that penalizes material inter-penetrability. If the contact surface is assumed flat, this may be achieved by using a signed distance ($\boldsymbol{n}$: normal vector, $\boldsymbol{x}_c$: a point on the flat surface, $\boldsymbol{x}_m$: the point that contacts the surface):

$$d = -\boldsymbol{n}^T (\boldsymbol{x}_m - \boldsymbol{x}_c) \tag{6}$$

Taking into account the expression in d, it turns out that *d>0* is an admissible region, while *d<0* is the admissible region. As a consequence, a potential function for simulating contact may be expressed as:

$$U^c = \frac{p}{q} < d >^q \qquad (7)$$

with *p* a penalty parameter, and *q* an exponent. The operator $< d >$ is 0 when $d < 0$, and equal to *d* otherwise. The value $q = 2$ is a common choice, but gives rise to non-smooth derivative (forces) at $d = 0$, while for $q = 3$ the function $g^c = \nabla U^c$ is C^1 for d = 0, giving better convergence properties.

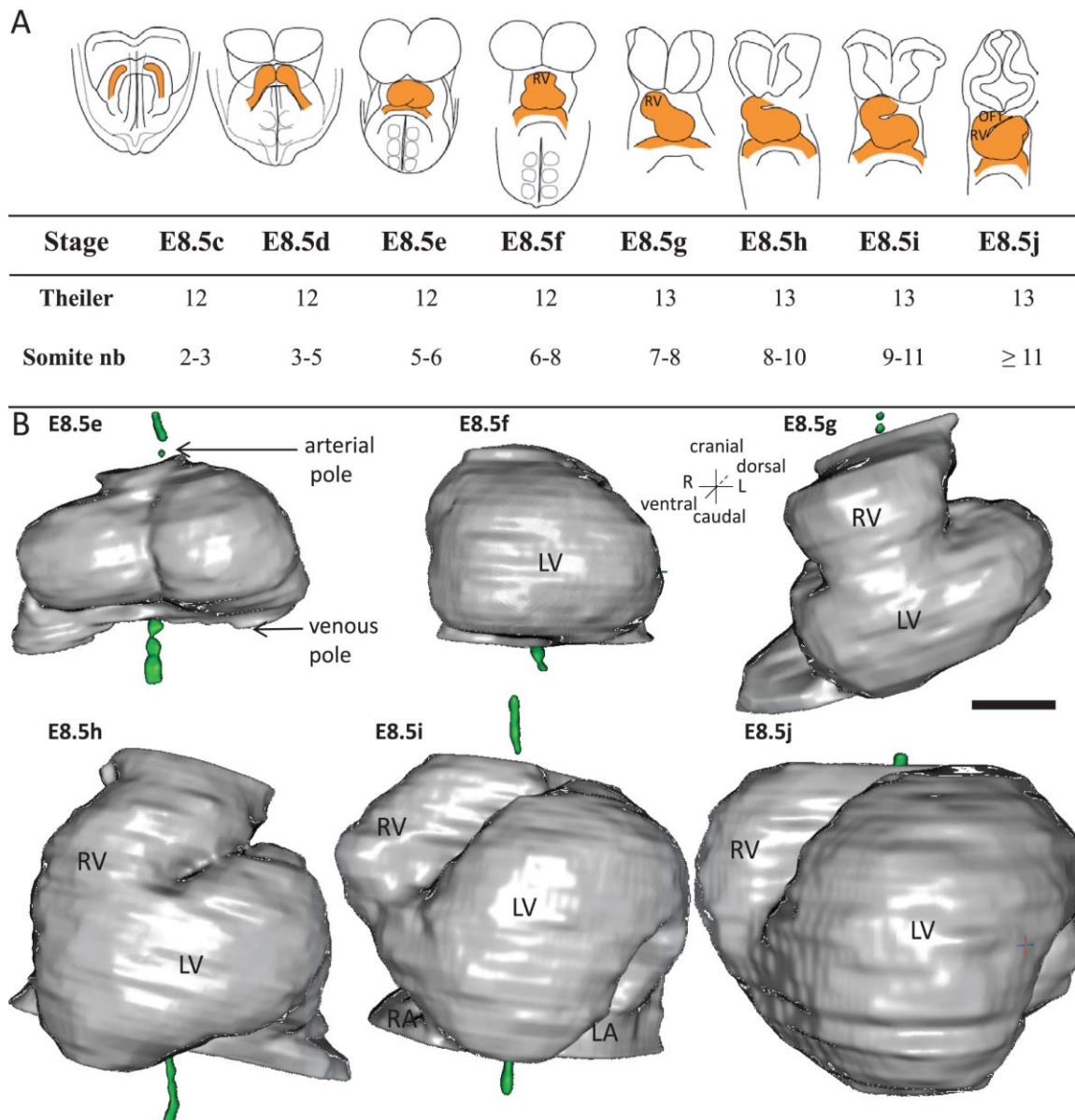For the solution of the non-linear equation $g^e + g^c = 0$ we use the Newton-Raphson process.

Aims of the study

Following this line, in this project we wanted to develop an analysis of the asymmetric right-left pattern in the morphogenesis of the mouse heart, based on the data provided by a simulation from images obtained by high-resolution electron microscopy (HREM) of the mouse embryo with a growth of 9.5 hours of development. The specific objectives of the study were the following:

- To carry out a discretization of the tubular geometry of the heart using finite element techniques.
- Apply the boundary conditions and non-isotropic growth parameters to evaluate the orientation of the buckling process.
- Simulate the cardiac loop for visualization and comparison of experimental images.

RESEARCH METHODOLOGY

Our data are based on a novel staging system for early cardiac development, based on the shape of the heart tube. It consists of eight stages of formation (Fig.3) and, to better characterize the shape changes during the cardiac loop, 3D images were acquired and reconstructed according to the different developmental moments of each stage. Of these, the E8.5g stage is particularly interesting, as this is where the first sign of left-right asymmetry occurs, with the tilting of the tube axis. Our model is based on state **8.5i-8.5j**, with a morphogenesis development of 9.5 hours.

Stage	E8.5c	E8.5d	E8.5e	E8.5f	E8.5g	E8.5h	E8.5i	E8.5j
Theiler	12	12	12	12	13	13	13	13
Somite nb	2-3	3-5	5-6	6-8	7-8	8-10	9-11	≥ 11

Figure 3. Stages depicting the progression of heart looping in the mouse. (A) Schematic representation of shape changes during the formation and looping of the heart tube (orange) in the E8.5 mouse embryo. (B). 3D reconstructions of heart shapes from HREM images at each stage of heart looping. All the reconstructions are aligned with the notochord vertical (green), the arterial and venous poles up and down, respectively. L, left; LA, left atrium; LV, left ventricle; OFT, outflow tract; R, right; RA, right atrium; RV, right ventricle. Scale bar: 100 mm (Le Garrec et al., 2017).

The file type we have worked with is STereoLithography, abbreviated as STL. This format defines the geometry of the 3D objects, excluding colour, texture or physical properties that are present in other CAD formats. The format includes the surface mesh of triangular elements with three nodes per element.

First, we pre-process our STL model, i.e. the first objective is to apply a correct volumetric discretization through finite element techniques.

Data pre-processing

It is common for this type of models to have a large number of elements and nodes, and they do not always form a closed surface structure, but rather have certain "loose" elements or nodes that prevent the creation of the volume of the surface system.

● **Mesh reduction and cleaning with *Autodesk MeshMixer***

This pre-processing was started with the Autodesk MeshMixer tool. This is one of the free 3D software products offered by Autodesk, which offers several useful features for 3D modeling and printing. The software is available for Windows and Mac OS and is based on surface modeling. With it, you can design any type of part based on another model, more precisely in a triangular mesh. The menu available in this tool is more extensive, of which we will highlight the following (Fig. 4):

Selection. On the left is the main panel. You can toggle between Brush and Lasso at the top. Lastly, we have the Size slider, which simply adjusts the size of the Brush/Sphere.

- ctrl/cmd + g - Create a Facegroup. This key assigns a new Facegroup to the selected triangles.
- Double click. The entire Facegroup, which is what we have made for our model, will be added to the selection.
- Delete. This will simply delete any selected faces.

Edit. Through this panel, we can reduce the mesh of our model uniformly, acquiring a smaller number of elements and nodes. By setting a specific reduction percentage we can then export the STL file in either binary or ASCII format.
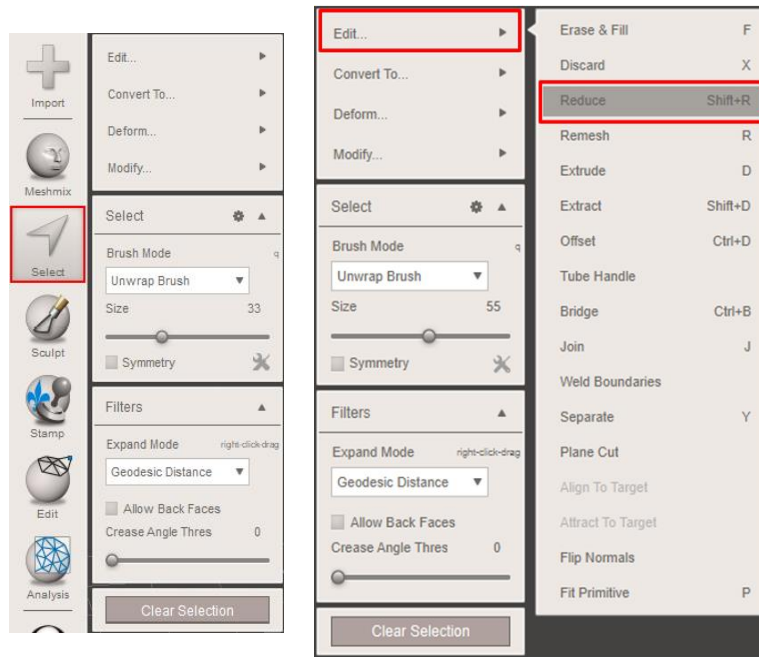
Figure 4. Main menu tools in Autodesk Meshmixer.

We performed a reduction of the surface mesh, which initially had a total of 459147 nodes and 918314 triangular elements. This procedure was performed in two steps:

- Target reduction of 80% of uniform type and preserving the boundaires.
- Re-target reduction of 30% with identical characteristics.

The surface mesh was left with a closed configuration, without errors and with a total of 41773 nodes and 83566 elements (Fig. 5). The file was exported in the same STL format.
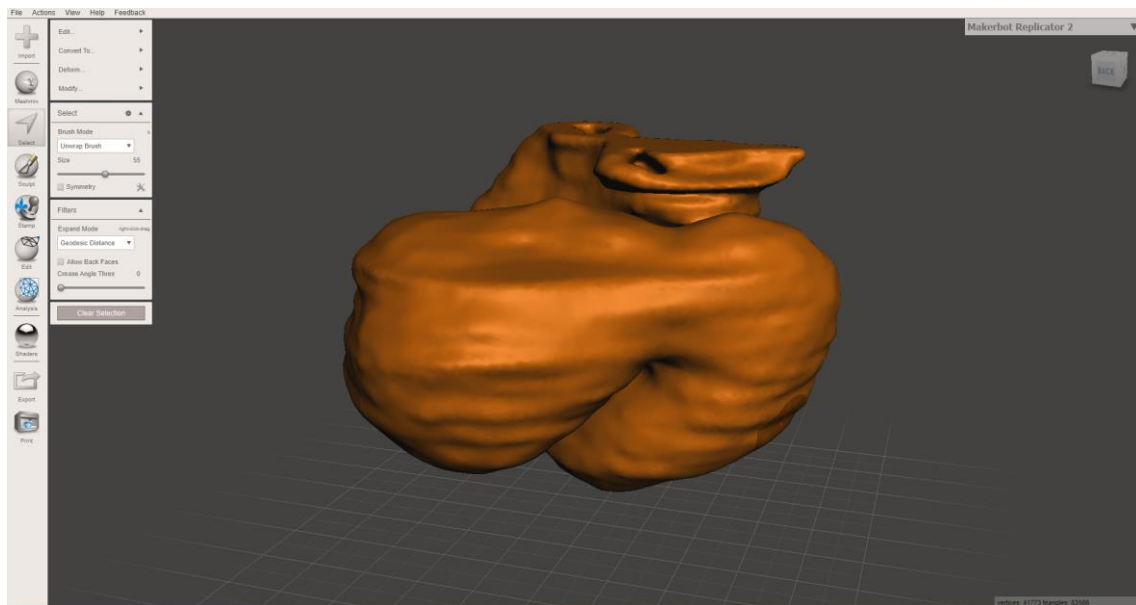

**Figure 5**. STL model after 80-30 reduction of the surface mesh.

● **Mesh volume and discretization with *Gmsh***

Once the surface mesh reduction was done, we proceeded to obtain the mesh volume of our model. To do so, we used the Gmsh software. Gmsh is an automatic 3D finite element mesh generator with solution and post-processing modules. Christophe Geuzaine and Jean-François Remacle first developed it as academic software, but it has become a useful tool in these environments (Geuzaine and Remacle, 2009). The Gmsh program is free, cross-platform, and written in C++. It contains four modules:

- ❖ Geometry. Using this module, it is possible to draw points, lines, surfaces, and volumes in order to create a desired figure. With *.geo files, these geometries can be imported or exported.

- ❖ Mesh. This is the main function for which it was developed. Within this module, Gmsh comes with 1D, 2D, and 3D meshing algorithms. The algorithm has user-adjustable parameters such as element size intervals, the minimum number of points to mesh, etc. There are options to generate triangles and quadrilaterals in 2D as well as tetrahedra, hexahedra, prisms, and pyramids in 3D. We have primarily used this module for our data.

- ❖ Solver. A finite element solver module that calls external systems to interact with in order to solve a finite element problem.

- ❖ Post-processing. This module includes a large number of alternatives in terms of visualization, differential and vector operations and data export functionalities.

Once our model was reduced, we obtained the volume of the STL mesh, for which we used the Geometry and Mesh menu. The result was a mesh volume of 311515 elements and 71518 nodes in total (Fig. 6), with which we exported the file in *.m format for further processing in Matlab.
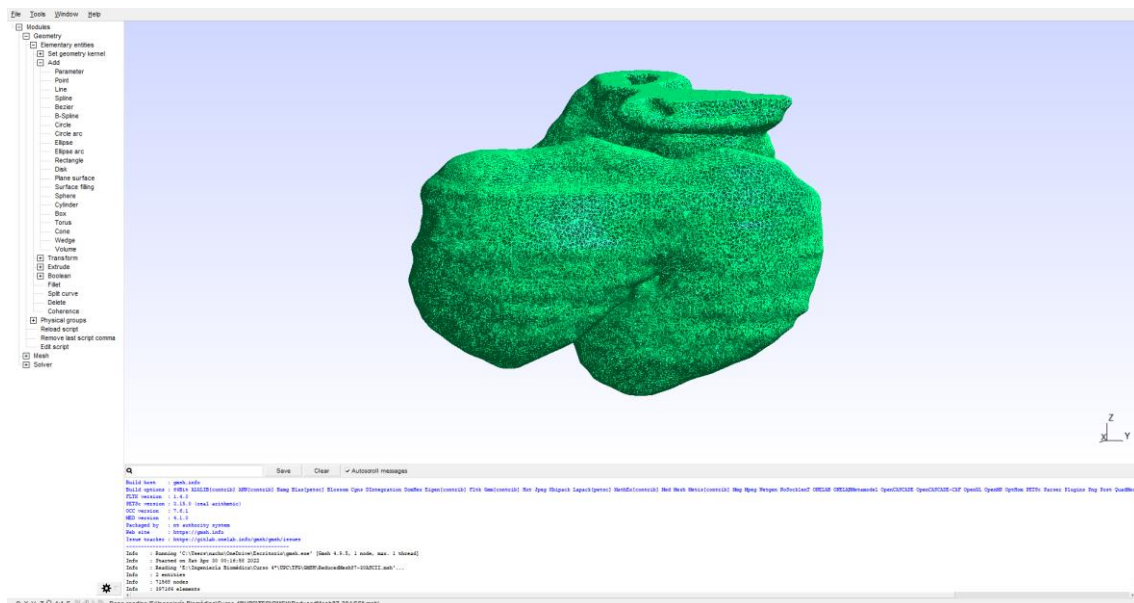
**Figure 6**. Representation of the optimized mesh of the volume and surface of the STL model.

Data processing

After pre-processing our model data, we used Matlab and GiD software to develop the viscoelasticity problem, apply boundary conditions, establish growth and perform a subsequent analysis of results depending on whether these parameters were set globally throughout the heart or locally to simulate and predict growth based on these parameters.

● **Import into *GiD* and boundary conditions**

The GiD software is a universal, user-friendly, adaptive preprocessor and postprocessor for numerical simulations in science and engineering. From pre- to post-processing, it has been designed to meet all the needs of the community in the field of numerical simulation.

Through this environment we apply the appropriate refinements to our mesh. In particular, we established the boundaries of the different structures of the heart, to which we then applied boundary and boundary conditions to set specific growth parameters. This division consisted of five areas: RV, right ventricle (red); LV, left ventricle (blue); RA, right atrium (pink); AVC, atrioventricular canal (yellow); OFT, outflow tract (green) (Fig. 7). We established in GiD the rigid material and the soft material, i.e., the right ventricle as rigid material and the OFT as soft material, since this is the area where no growth will be applied.
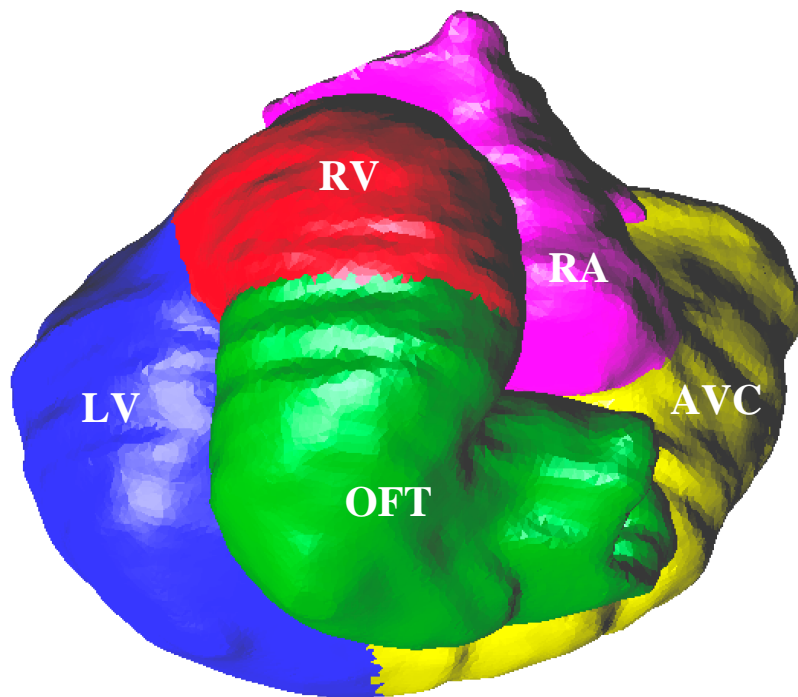
Figure 7. Representation of the model in GiD with the five regions marked and plotted to which different growth magnitudes are applied in the simulation. RV: Right Ventricle; LV: Left Ventricle; OFT: Outflow Tract; AVC: Atrioventricular Canal.

● **Data processing in** *Matlab*

Once the separation of structures has been applied, we carry out all the processing of the different models in Matlab based on the parameters mentioned above. This program is a numerical computing and programming platform used by millions of engineers and scientists to analyze data, develop algorithms, and create models. It could be said that it is one of the most used programming languages today.

It is worth remembering that there is a distinction between specified growth, which is the growth that would be obtained if each region grew independently of its neighbours (i.e. in mechanical isolation), and the resulting growth, which is the growth that is observed when the mechanical constraints of its neighbours are taken into account (i.e. the mechanically connected tissue). Understanding the mechanisms by which the resulting growth arises therefore requires knowledge of how genes influence the specified growth. When the specified growth is isotropic, genes have to control a single parameter, which is the local growth rate. However, in many cases specified growth can be anisotropic, requiring both growth orientations and growth rates to be under genetic control. Control of growth orientations requires the definition of a local axis (i.e. axiality, represented as a field of lines). In this sense, growth is similar to strain, which also has axiality. This similarity has led to the suggestion that tensions provide the main keys to guide growth. According to this tension-based axiality mechanism, gene activity influences tissue tensions, the orientations of which are transmitted to influence the molecular properties of cells, such as the cytoskeleton. These, in turn, modulate growth orientations, which in turn can influence the pattern of stresses. In this regard, we have developed a series of simplified hypothetical models that illustrate how growth and polarity can interact combinatorially during morphogenesis to generate a set of different shapes, with left-right asymmetry depending on the angle of orientation. (Kennaway et al., 2011).

Finite Element Method (FEM) modelling of linear/non-linear viscoelastodynamics with growth

During each simulation step, each element is deformed according to a growth tensor field defined from the hypotheses of the model. The constraint of continuity of the tissue implies that the resulting growth is different from the input growth, causing residual strain. Simulations are run using linear elastic assumptions to compute the output shape by minimizing residual strain energy (see Annex A.2-A.5).

In a first model, growth was established in all described regions without applying a specific constraint. In a more refined model, the OFT was simulated as a displacement constraint on a set of nodes located along the output of the OFT (Fig. 8). These nodes were not allowed any displacement along the x, y and z axes.
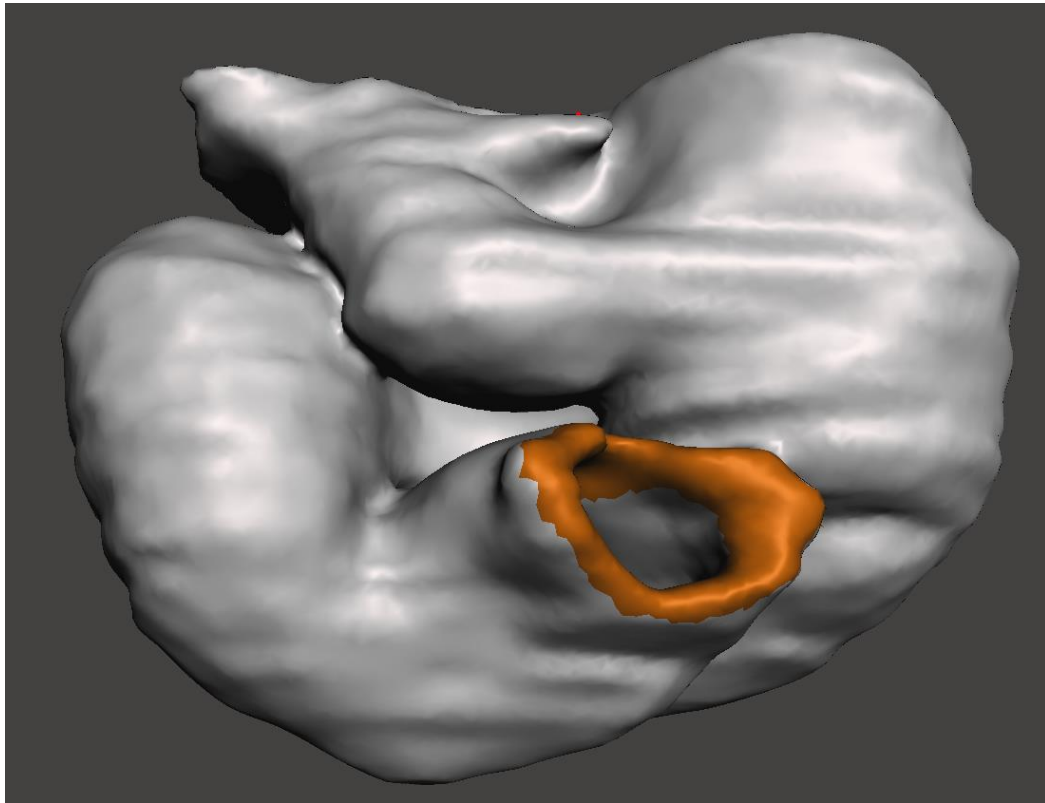
Figure 8. Illustration of the heart showing the OFT bounded region in orange, where no x-y displacements are allowed.

The input parameters for growth were established as follows (see Annex A.6):

1. The basic isotropic longitudinal growth, active in each heart element, was set to obtain a given increase in each region, so that if for OFT as a material a growth of 0.8 is set, it means that the size after the simulation will have increased by a factor of 1.8, i.e. 80% of its initial size. For the rest of the structures, the same process was carried out for both contact and non-contact models (Table 1 and 2). The corresponding value for the overall growth is 2% per time step.

2. A constraint applied in the OFT structure for non-isotropic growth, so that a null value of growth was introduced to avoid the displacement of the nodes, keeping the rest of the structures with the same amount of longitudinal growth (Table 1).

3. Isotropic growth with a magnitude higher than the initial values indicated in point 1 for the GrI and NGrI simulations (see Tables 1 and 2). These increases were, compared to the Gr and NGr simulations, by a factor of 1.8, which means that the size will grow by a factor of 2.8, i.e. by 180% for OFT. The same for all other structures in both the contact and non-contact models.

4. A constraint applied in the OFT zone, introducing a null value in a similar way to point 2, but maintaining the increments established in the previous point (Table 2).

Non-Contact		Growth					Steps
	Simulation	OFT	RV	LV	AVC	RA	
	Gr	0.8	1	1	0.7	2.1	50
	NGr	0	1	1	0.7	2.1	50
	GrI	1.8	2	2	1.7	3.1	50
	NGrI	0	2	2	1.7	3.1	50

Table 1. Set of the different simulations to evaluate the performance of the models as a function of the indicated parameters. Different growth values were tested on the structures, without taking into account the contact parameters, the OFT zone being the only one where no growth was applied for simulations NGr (Gr: Growth, NGr: Non-Growth, GrI: Growth Increased, NGrI: Non-Growth Increased).

Contact		Growth					Contact Parameters		Steps
	Simulation	OFT	RV	LV	AVC	RA	Contact A	Contact MS	
	GrC	0.8	1	1	0.7	2.1	1e-5	1	50
	NGrC	0	1	1	0.7	2.1			50
	GrIC	1.2	1.5	1.5	1.05	3.15	1e-5	1	50
	NGrIC	0	1.5	1.5	1.05	3.15			50

Table 2. Set of the different simulations to assess the performance of the models in terms of the parameters indicated. Different values of growth in the structures were tested, as well as the level of the contact parameters (Contact A and Contact MS), where the OFT zone was the only one where no growth was applied for simulations NGrC (GrC: Growth Contact, NGrC: Non-Growth Contact, GrIC: Growth Increased Contact, NGrIC: Non-Growth Increased Contact).

Simulations visualized in *ParaView*

ParaView is an open source, cross-platform data analysis and visualization software that provides the ability to build visualizations to analyze data using qualitative and quantitative techniques. Data exploration can be done interactively in 3D or programmatically through ParaView's batch processing. It uses the Visualization Toolkit (VTK) as the data processing and representation engine, the format in which we develop the different simulated models (Fig. 11).

RESULTS

As mentioned above, it is important to note the effect of contact between the mesh elements of our base model in different areas of the model. An alternative to adding a contact potential is to directly remove the existing one in the desired area. We know that these connections could cause irregularities when post-processing our data, so we proceeded to remove the contact elements using GiD. However, we realized that by removing this contact, the domains overlapped, which is not quite similar to reality, so it became necessary to incorporate the contact function into the programming of the simulations. For this reason, we decided to make a comparison between both types of configurations, with and without contact (Fig. 9).

For the contact configuration, we set up different functions so that the simulations could converge during their running for each increment. Among these, two parameters should be highlighted, the value of the penalty parameter of the potential function, which in the programmed nomenclature is set as "Contact A", so that the lower its value the easier the convergence will be since the contact forces are reduced; and the master parameter set as "Contact MS", since it tries to find the nodes at a minimum distance from the slave triangles. This means that for the value MS=1 only the contact of the nodes on one side is applied with respect to the contact of the opposite surface, for MS=2 the nodes and the surface are exchanged, and with MS=3 restrictions are applied on the nodes on both sides (see Annex A.1).

Evaluation and quantification of the Angle Twist

To assess the pattern of right-left asymmetry due to non-isotropic growth, we chose two representative pairs of nodes. Both were located in the RV and VI, one closer to the caudal region and the other closer to the cranial region. The nodes were sufficiently separated and coincided approximately in the plane of the x-axis. In each simulation obtained, we quantified the vectors linking each pair of nodes, so that we compared the angle between the two vectors from one simulation to another.

Non-Contact   **Contact**
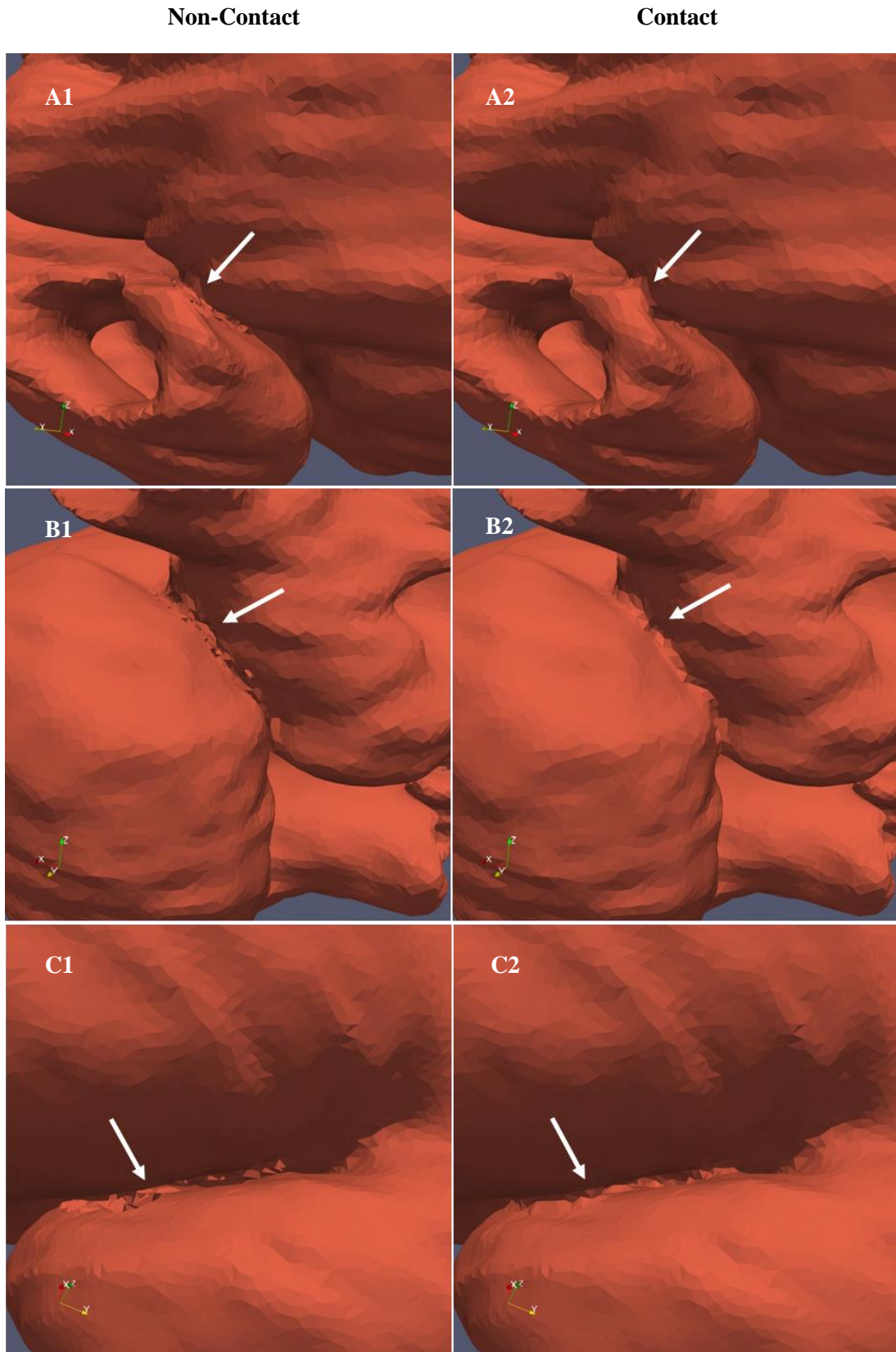
Figure 9. Contact and non-contact regions. A1-A2) contact and non-contact between OFT and AVC regions; B1-B2) contact and non-contact between RV and RA regions; C1-C2) contact and non-contact between RV and OFT regions.

● **Non-Contact Models**

There was rotation between simulated models Gr-NGr, and between simulated models GrI-NGrI, with corresponding parameters. When counteracting the first two simulations, the maximum angle reached was 6.1338° on average, while for the next two, it reached a sharp rotation of 46.4923° on average, both measured in the plane of the ventral-dorsal axis for a growth of 49 steps (Fig. 10 and 11), as not all models converged on the proposed steps. According to these data, performing the two-sample t-test assuming unequal variances, a statistically high significant difference was obtained with a p-value of 3,36861E-20 (Table 3). The angle of rotation is positive, so that rotation is generated in the transverse plane (XY), along the cranial-caudal axis to the right (Fig. 14). A slight rotation is also observed in the coronal plane (YZ), along the ventral-dorsal axis to the left (Fig. 15).

	Compared simulations		Max. angle of twist	Steps	p-value
Non-contact	Gr	NGr	6,6142 °	49	3,36861E-20
			5,6535 °		
	GrI	NGrI	59,2287 °	49	
			33,7560 °		

Table 3. Determination of the maximum angle between each pair of simulations, as well as the p-value for the t-student test, as a function of the number of steps and the growth parameters set per model in Table 1.

NON-CONTACT
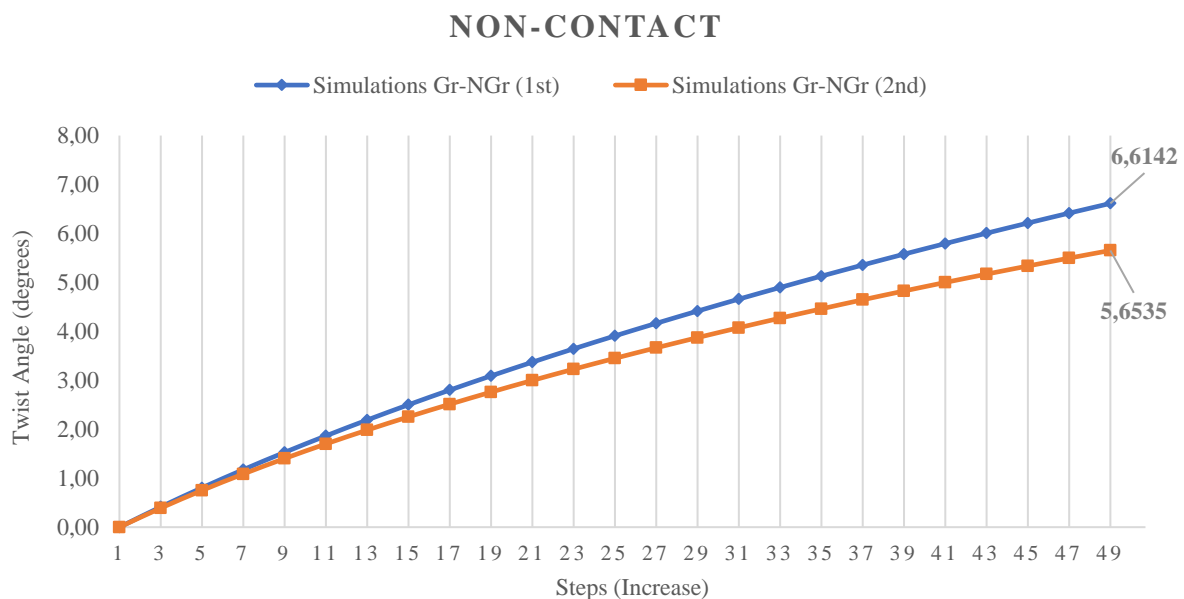
Figure 10. For both pairs of nodes in simulations Gr-NGr, the angle of twist is shown as a function of the growth increase.
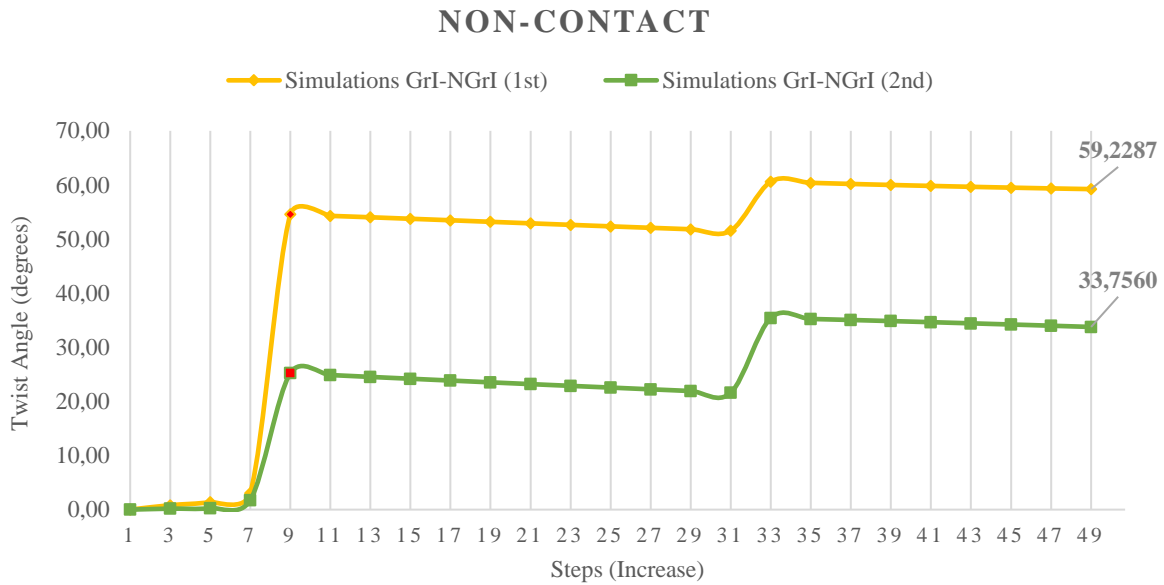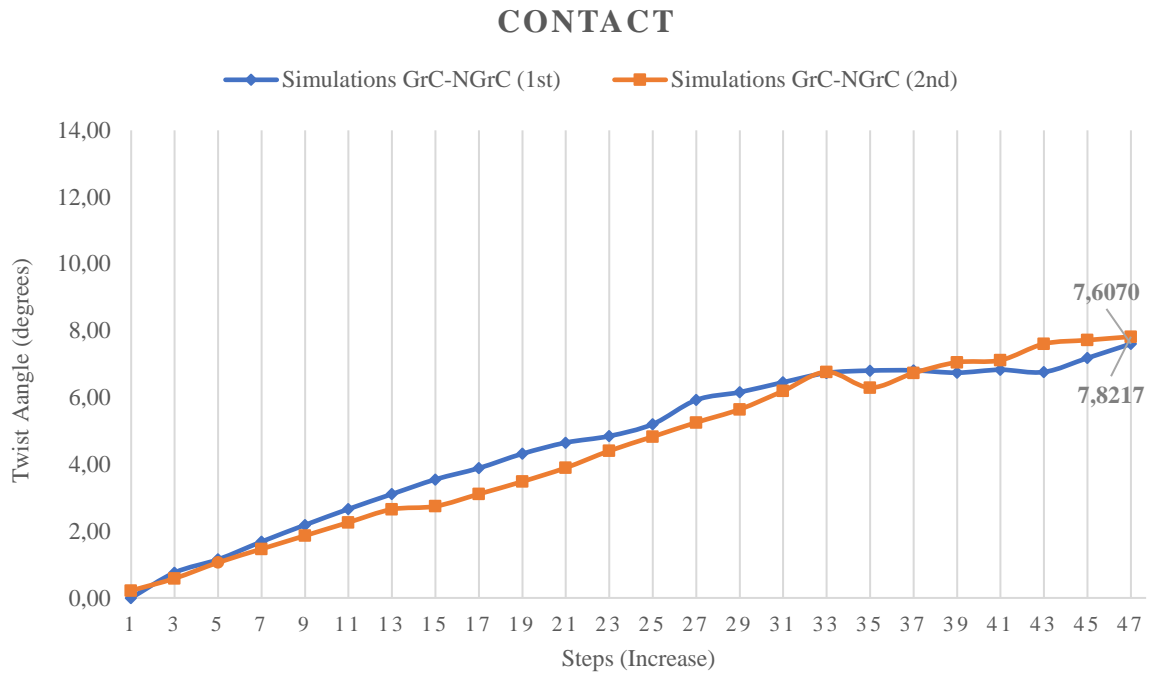
Figure 11. For both pairs of nodes in simulations GrI-NGrI, the angle of twist is shown as a function of the growth increase.
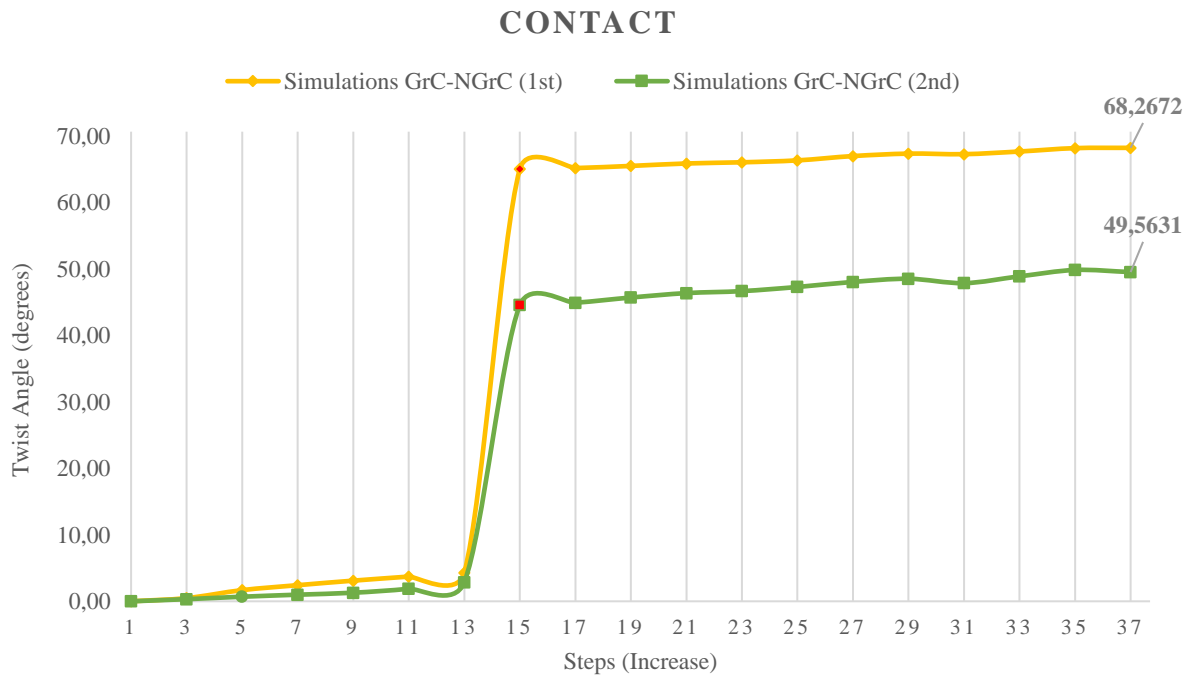
● **Contact Models**

For the simulations with contact there was likewise rotation between simulated models GrC-NGrC, and between simulated models GrIC-NGrIC with the corresponding parameters. By counteracting the first two simulations, we obtained a linear increase of the rotation angle, with a maximum reached for 47 increments of 7.6070º and 7.0103º for the representative RV-LV node pair measured in the plane of the ventral-dorsal axis (Table 4; Figure 12). In the case of GrIC-NGrIC, the rotation angle had a sharp difference from increment 13-15, although on this occasion the simulation converged until step 37. The maximum angle reached for the node pair was 68.2672º and 49.5631º, respectively, and in the same plane (Figure 13). For these data, a two-sample t-test (GrC-NGrC versus GrIC-NGrIC) assuming unequal variances yielded a clearly statistically significant difference with a p-value of 1.75049E-09 (Table 4). For the models with contact, the angle of twist is also positive, so that the rotation is generated in the same way in the transverse plane (XY), along the cranial-caudal axis to the right (Fig. 16). A subtle rotation can again be seen in the coronal plane (YZ), along the ventral-dorsal axis to the left (Fig. 17).

|	Compared simulations		Max. angle of twist	Step	p-value
Contact	GrC	NGrC	7,6070 °	47	1,75049E-09
			7,0103 °		
	GrIC	NGrIC	68.2672 °	37	
			49,5631 °		

Table 4. Determination of the maximum angle between each pair of simulations, as well as the p-value for the t-student test, as a function of the number of steps and the growth parameters set per model in Table 2.

Figure 12. For both pairs of nodes in simulations GrC-NGrC, the angle of twist is shown as a function of the growth increase.


Figure 13. For both pairs of nodes in simulations GrIC-NGrIC, the angle of twist is shown as a function of the growth increase.
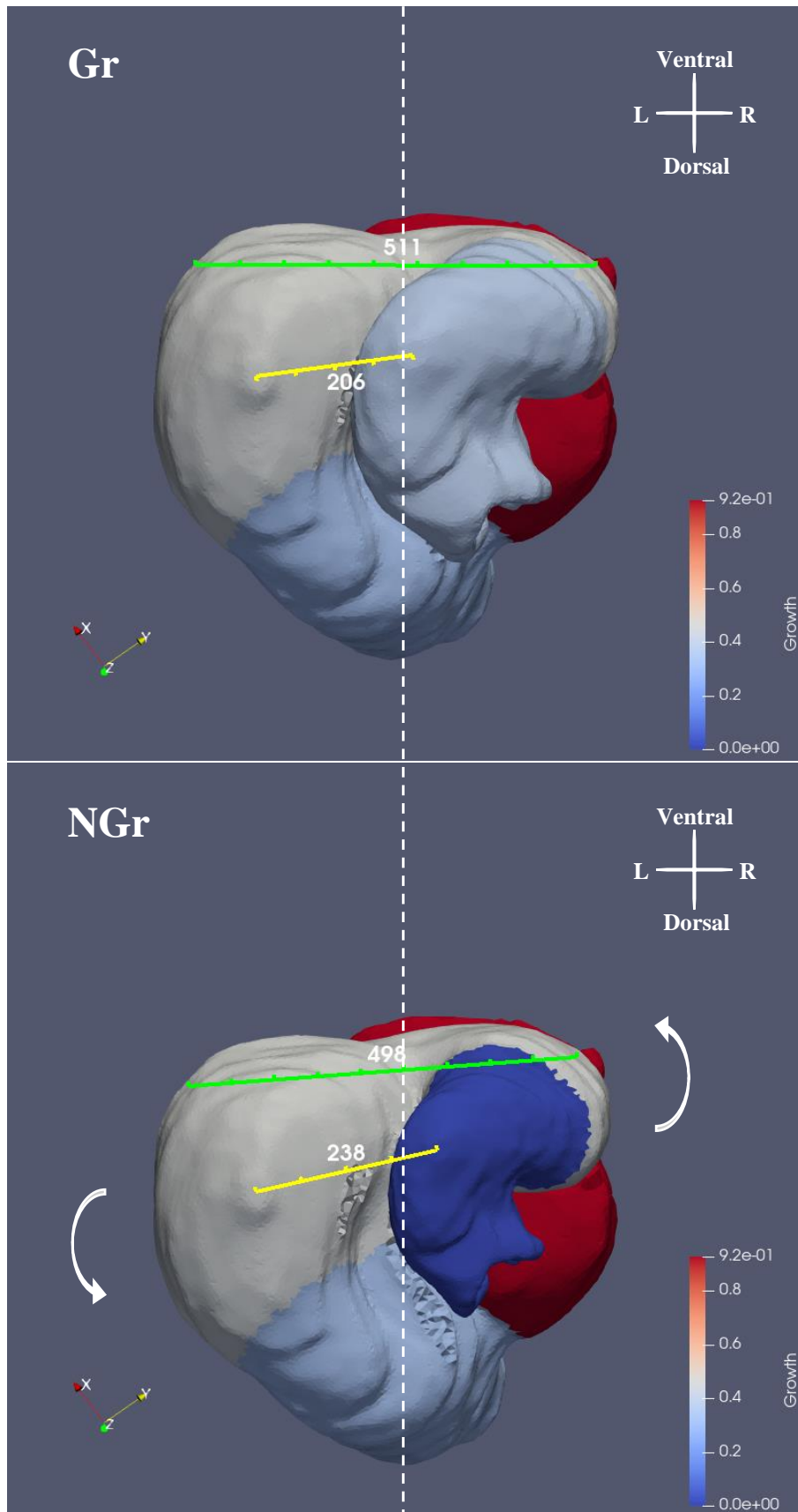
Figure 14. Illustration of the models at simulation increment 22 (A) Non-contact Gr model; (B) Non-contact NGr model. Both images were captured in the transversal plane (XY) where the variation of both rotation angle and distance can be observed between the representative RV-LV nodes (green line) and an extra pair of nodes between OFT-LV (yellow line).
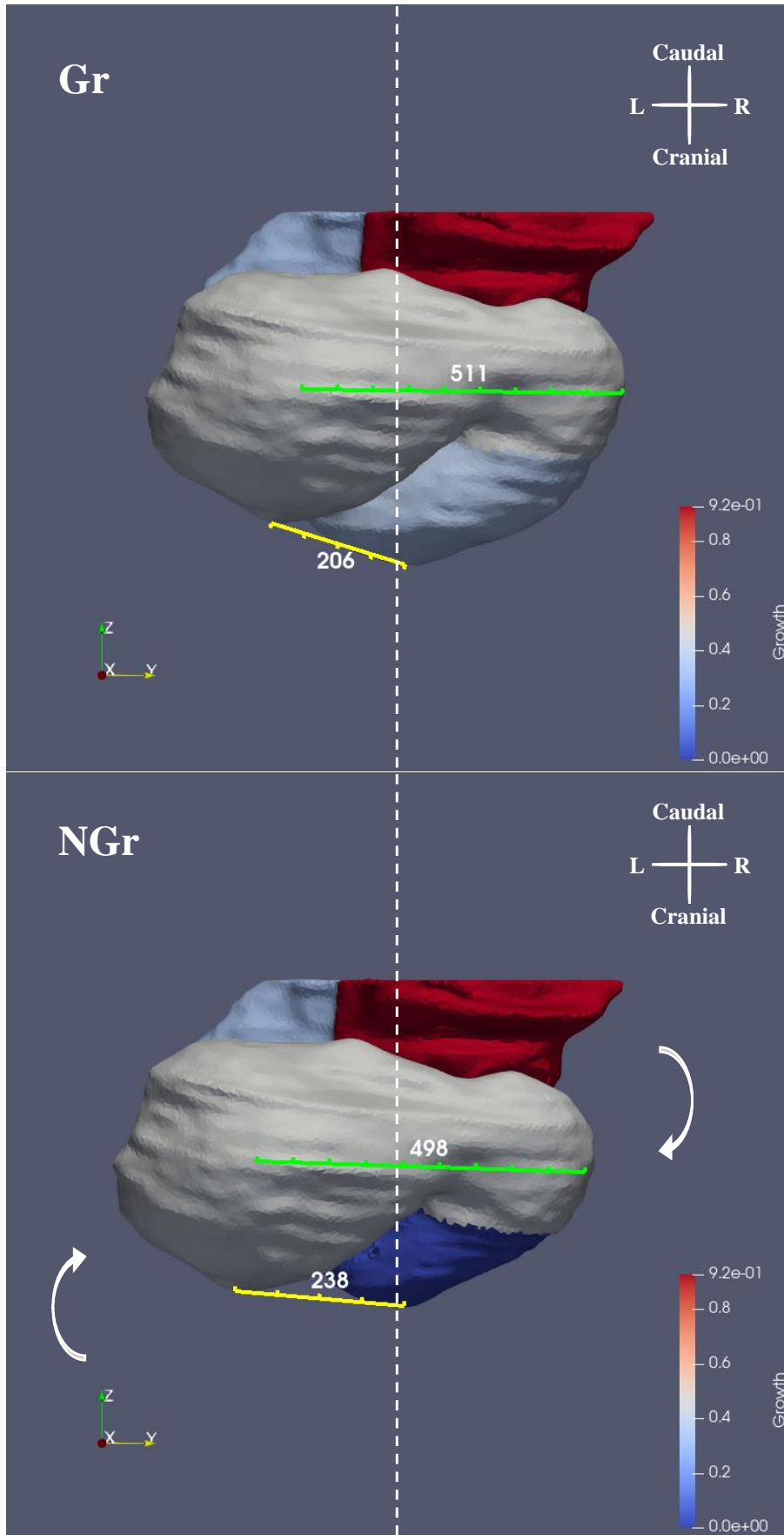
Figure 15. Illustration of the same models as in figure 13. Here we can see the coronal YZ plane, with the rotation (albeit more subtle) on its caudal-cranial axis between the representative nodes.
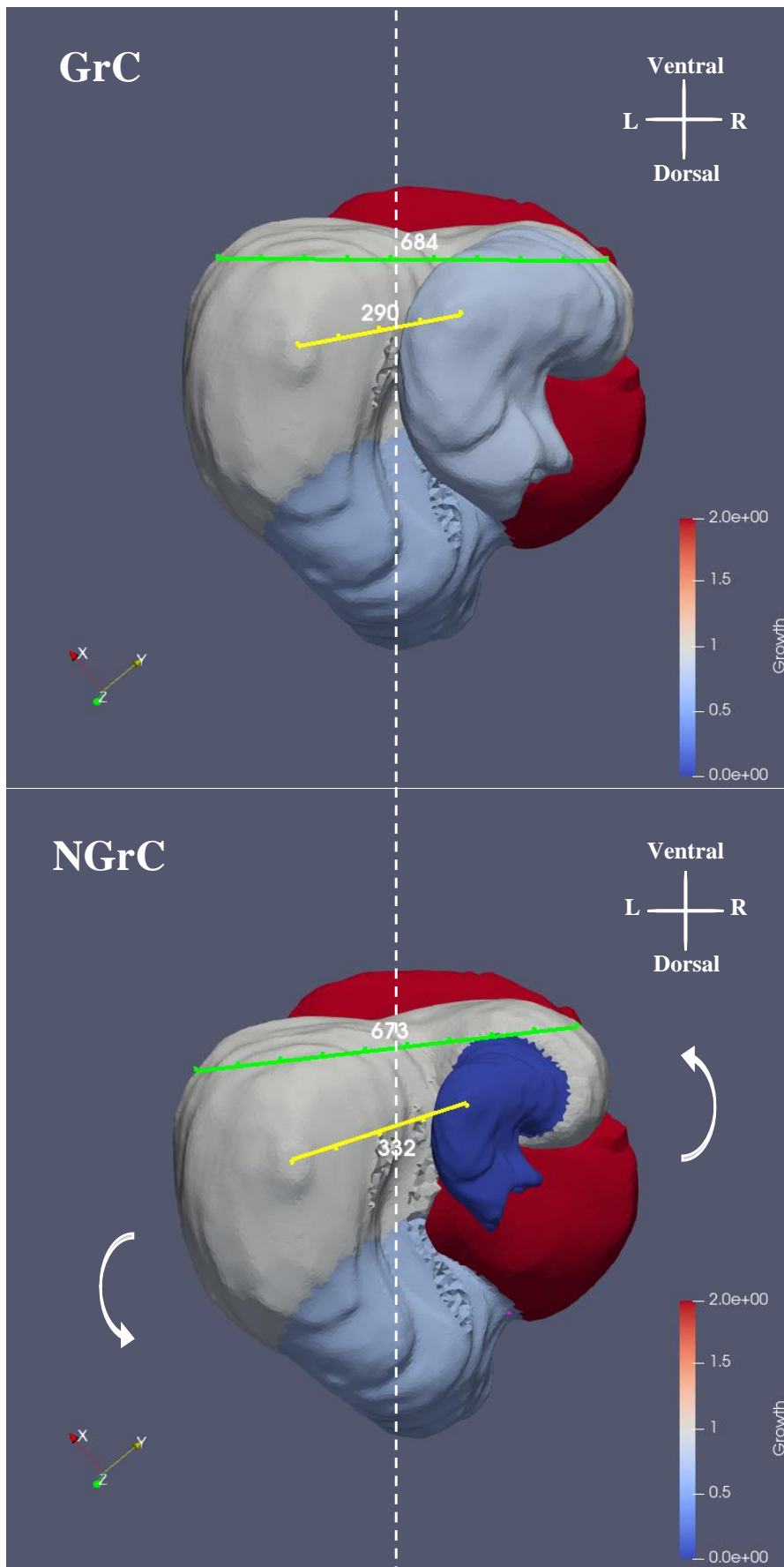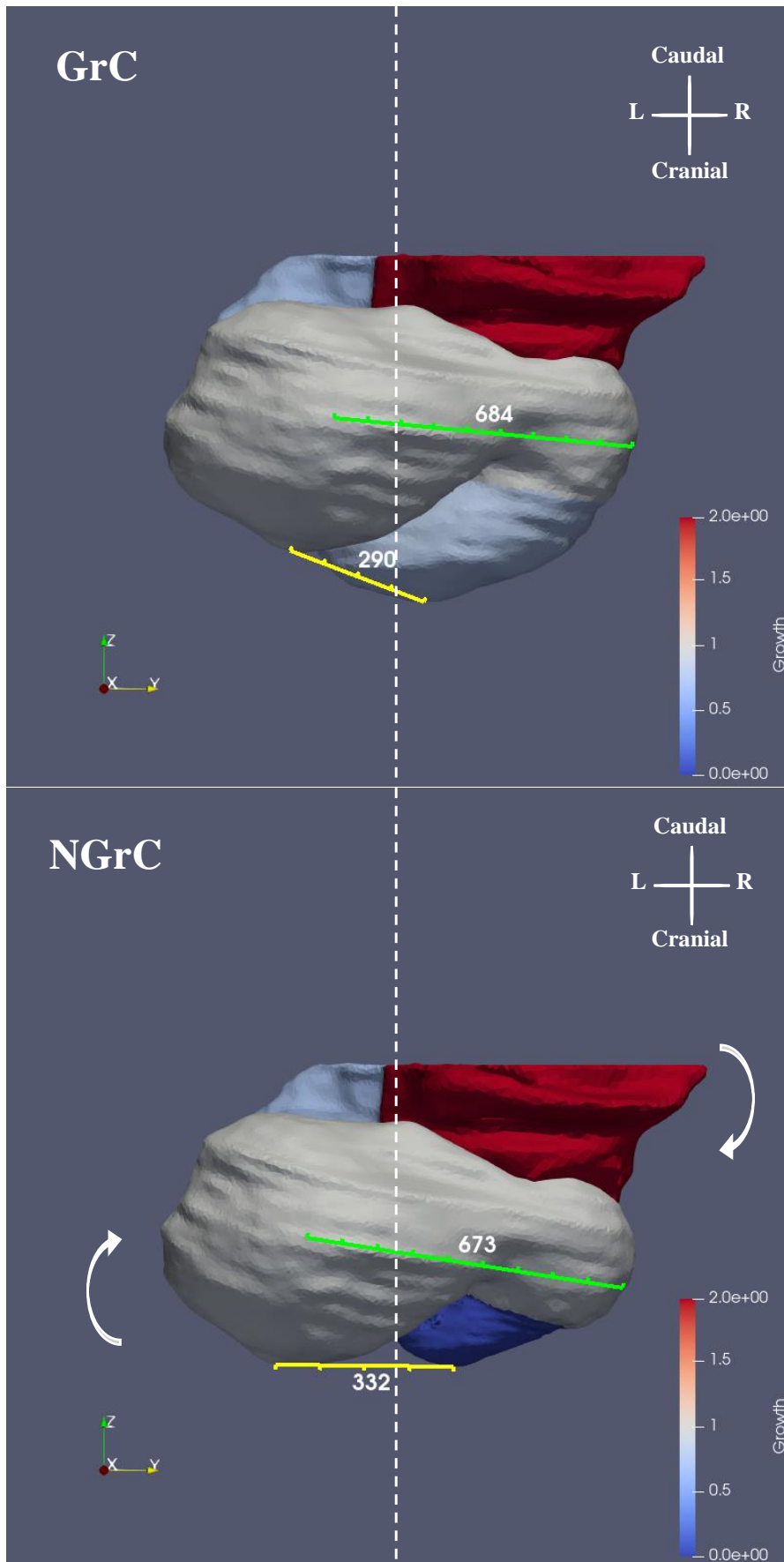
Figure 16. Illustration of the models at simulation increment 47: (GrC) Contact Gr model; (NGrC) Contact NGr model. Both images were captured in the same transversal plane (XY) where the variation of both rotation angle and distance can be observed between the representative RV-LV nodes (green line) and an extra pair of nodes between OFT-LV (yellow line).

Figure 17. Illustration of the same models as in figure 15. Here we can see the coronal YZ plane, with the slight rotation on its caudal-cranial axis between the representative nodes. This time the advancement of the RV over the LV can be seen to a greater extent.
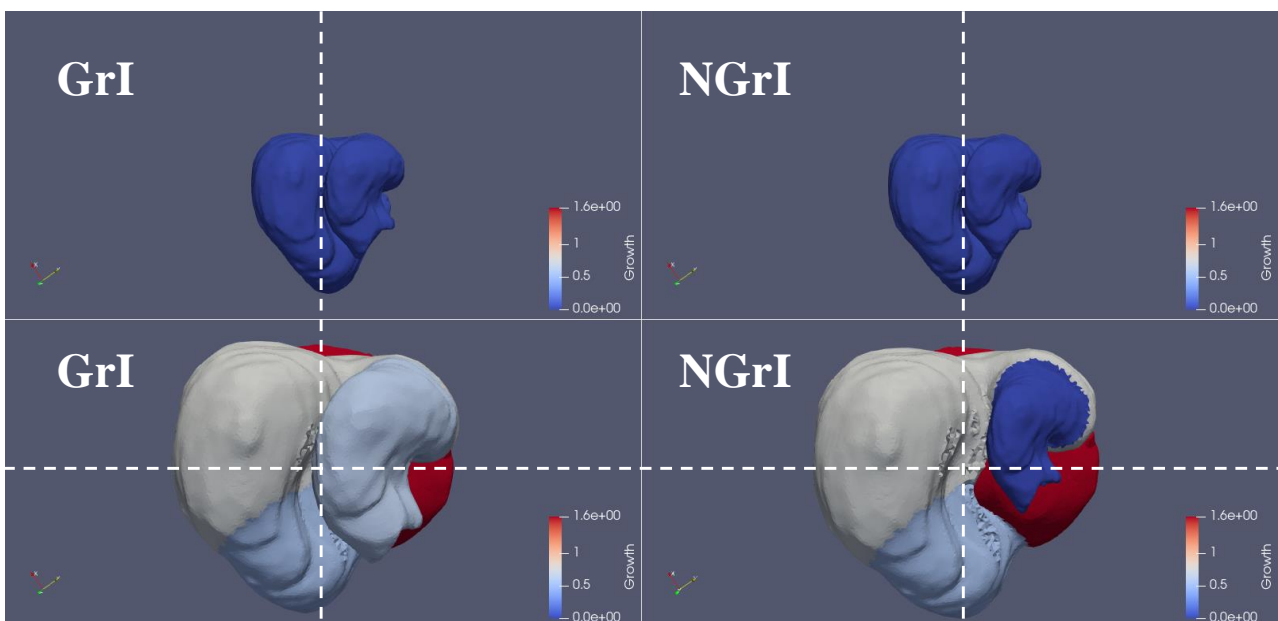
● Non-Contact vs Contact

The following graph (Fig. 18) shows the overall differences in the rotation angle for the first vector for the contact and non-contact simulations. In general, the sudden change is observed in both types when the growth of the simulation is higher (Gr → GrI and NGr → NGrI). However, we can see that the differences between the models with OFT and without OFT growth are only high when we apply a higher increment, i.e. for GrI-NGrI, in both contact and non-contact simulations. Nevertheless, this is not seen visually (Fig. 19 and 20).
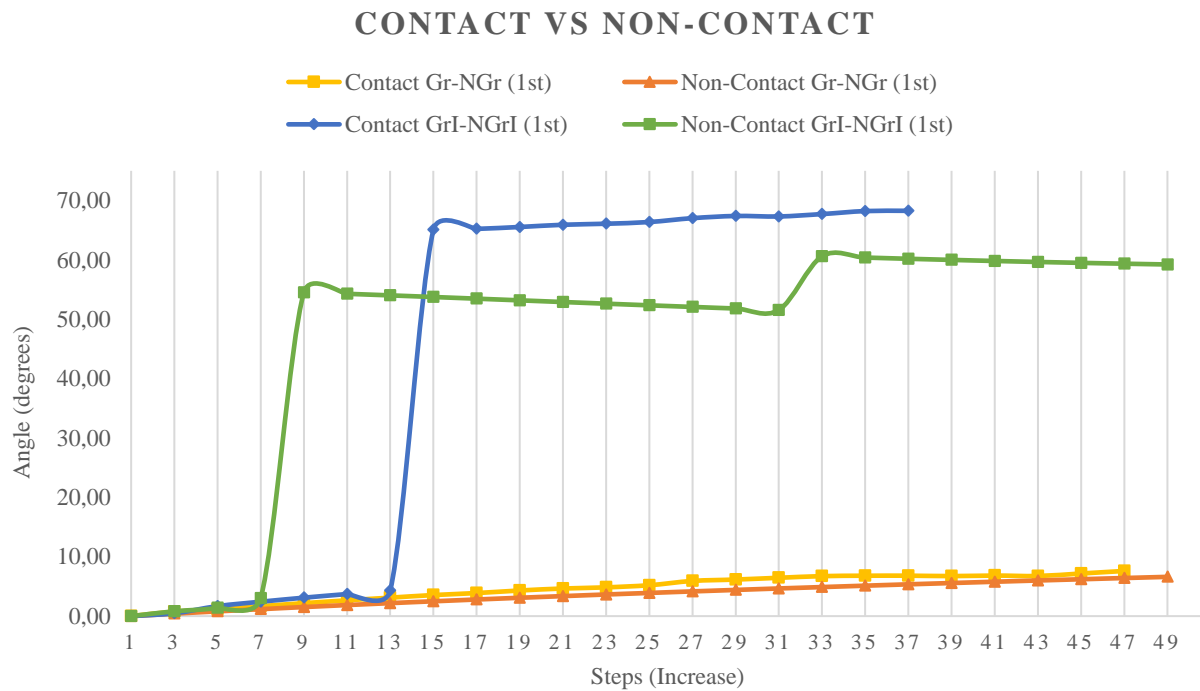
Figure 18. Comparison of the angle of rotation as a function of the increment between the simulations with and without contact, for the models with and without growth in the first vector (pair of nodes) analyzed.

Figure 19. Illustration of the transverse plane (XY) of the non-contact models between increments 1-37 for GrI-NGrI simulations. The angle of rotation can be seen, albeit slightly in comparison to that observed in the numerical quantification.
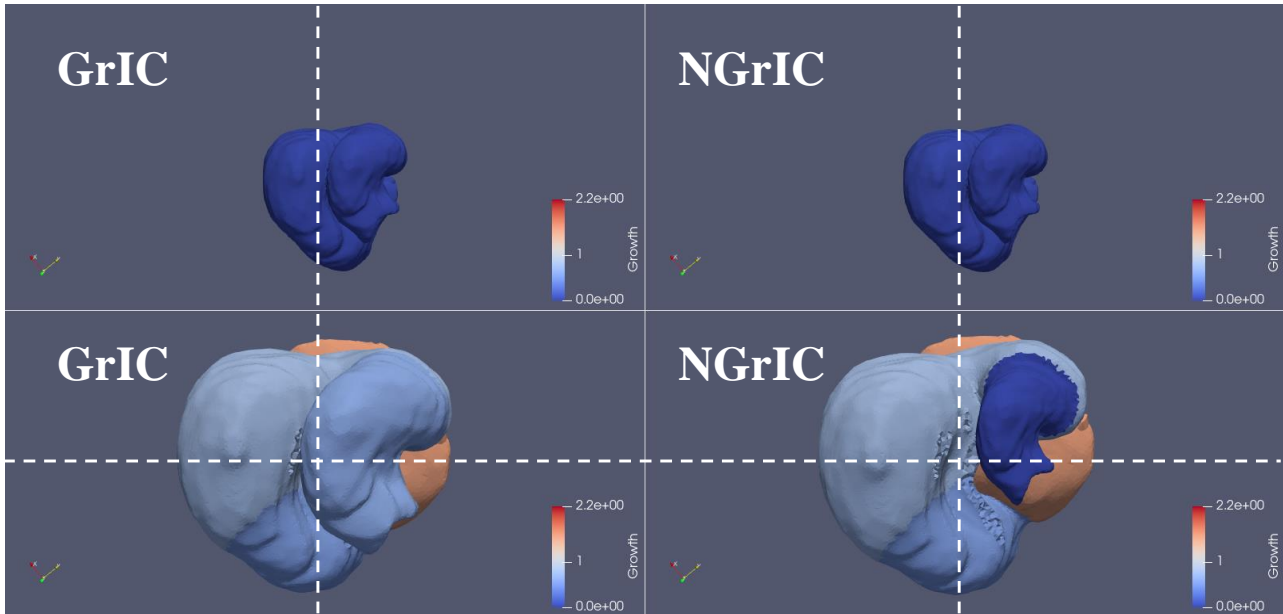
Figure 20. Illustration of the transverse plane (XY) of the models with contact between increments 1-37 for the GrIC-NGrIC simulations. The angle of rotation can be seen, albeit slightly in comparison to that observed in the numerical quantification.

DISCUSSION AND CONCLUSIONS

We have performed a 3D reconstruction of the growth of the mouse heart loop in different models, in which a certain region known as the outflow tract (OFT) did not support development, leading to an analysis of what kind of left-right asymmetry is generated in the formation of the heart in this case. For the simulations with the contact removed in certain areas of the mesh we applied non-isotropic growth in the five regions, where the results obtained indicate that there is a rotation during heart development when the heart size grows according to the Gr-NGr data (Table 1). This rotation leads to a more asymmetric development of the RV and LV, with the RV being more anteriorly positioned due to the non-growth of the OFT. This asymmetry was considerably greater when the increase in heart size was simulated more steeply, i.e. as a function of the GrI-NGrI data (Table 1), which leads us to believe that this abrupt difference between one applied growth and the other is due to the inaccuracy of the functions in the simulation, as well as the elimination of the elements in the contact zones.

In the case of the simulations with contact, where it was decided to develop the necessary functions so that the simulation could converge in these areas during the model increments, the rotation was generated with the same tendency as in the previous case for GrC-NGrC (Table 2), although with a slight increase in the angle (Table 4). Similarly, the asymmetry was even greater when applying the final size increment after simulation (GrIC-NGrIC), with the angle differences being statistically significant to a large extent, although for these models the percentage increase of the structures was smaller than in the case of the non-contact simulations. This led us to believe that, although the simulations after contact was applied converged better and gave a more realistic result, they did not accurately meet our goal of quantifying the rotation angle precisely.

It should be noted that in the development of the code and its optimization, it would be necessary to smooth the contact areas after reduction in the mesh of the heart of the starting model, leading to better convergence and a more rigorous simulation for each increment. Furthermore, it is important to note that for all simulated models certain oscillations were obtained during the increments, especially for the GrI-NGrI case, hence considerable differences were found between the quantified pairs of nodes.

In spite of the uncertainties that are revealed throughout each simulation, it is clear that the trend in left-right asymmetry during heart morphogenesis for a limited growth interval when the OFT region does not develop is rotational, so that the RV is tilted towards a position further forward with respect to the LV in the ventral direction.

The simulations are captured for a total of 50 increments, but in view of the results obtained this segmentation of the development time could be increased to 70-10-150 or other values in order

to assess how the rotation arises more thoroughly, bearing in mind that this change would entail a higher computational cost.

Clinical issues

Although there are multiple defects of laterality in the development of the heart, the heterotaxia syndrome is one of the most striking, as has been discussed. In fact, in 90% of cases it is associated with congenital cardiac defects and with considerable complexity. It is noteworthy that in 17.5% of cases of heterotaxy, the global situs of the heart is right-sided symmetrical, i.e. right isomerism, and this is associated to a greater extent with congenital heart defects such as complete atrioventricular canal defect or transposition of the great arteries and bilateral sinus nodes, among others (Lin et al., 2014; Mishra, 2015). On the other hand, if we look from a genetic perspective, heterotaxia is strongly associated with mutations in genes such as MMP21 or ZIC3, which are involved in node formation, being the embryonic left-right organizer where lateral symmetry is first broken.

Therefore, heterotaxia is associated with a randomization of the left-right pattern with a high discordance between the different anatomical structures. Finally, we highlight that transposition of the great arteries (TGA), a defect associated with heterotaxy, is a severe congenital heart defect in which the two blood circulations run in parallel, resulting in hypoxia of the systemic blood (Fig. 21). This defect, according to studies, may be the result of defective outflow tract rotation (OFT), which is a rightward process like the one discussed above. This indicates one of the possible manifestations of heterotaxy when the heart undergoes abnormal development of this cardiac structure, among others.
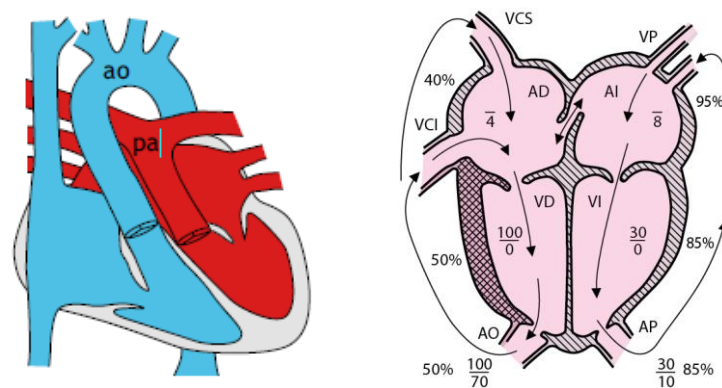
Figure 21. Left: Transposition of the Great Arteries (TGA), the positions of the pulmonary trunk and aorta are inverted (Desgrange et al., 2018); Right: Dextro-transposition of the great arteries, non-oxygenated blood returning to the right heart enters the AO, causing severe cyanosis. Oxygenated blood returning to the LA enters the pulmonary circulation again. There is hypertrophy of the right ventricle, and the foramen ovale allows mixing but mixing is inadequate. Atrial pressures are mean pressures. AO = aorta; IVC = inferior vein cava; LA = left atrium; LV = left ventricle; PA = pulmonary artery; PV = pulmonary veins; RA = right atrium; RV = right ventricle; SVC = superior vein cava (Lee B. Beerman, 2020).

BUDGET AND ECONOMIC ANALYSIS

This section specifies the costs associated with the preparation of the study, as well as the costs related to the future implementation of the models developed for the analysis of other diseases or malformations in the heart. The costs are broken down into the following groups:

- Human working hours
- Materials
- Software licenses

The value of the costs associated with the purchase of the material necessary for the implementation of the elaborated models presented in this budget coincides with the retail price supplied by each of the manufacturers. Likewise, the value of the costs of the various software licences specified in this budget coincides with the value of the sales price to private users. Therefore, all the cost values specified are duly referenced.

Human working hours

The manpower is divided into engineering, supervisory and technical according to the nature of the tasks performed and/or proposed, these being conceptual development, development management and model implementation, respectively (Table 5).

Staff Type	Quantity (h)	Unit Cost (€/h)	Total Cost (€)	Subtotal (€)
Engineering	350	12,00	4200,00	
Supervision	50	24,00	1200,00	**5760,00**
Technical	40	9,00	360,00	

Table 5. Human working hours costs.

Material

Table 6 below shows the costs associated with the acquisition of the material necessary to carry out the study.

Material Type	Concept	Quantity	Unit Cost	Total Cost (€)	Subtotal (€)
Laptop Computer	HP ENVY 15-ep1015ns	2	799,00 (€/u)	1598,00[a]	
Documentation	Books, Papers, etc.	1	50,00	50,00	**1717,12**
Cluster Computer	LaCàN HPC Beowulf cluster	1	0,12 (€/h)	69,12[b]	

Table 6. Material costs.

(a): The cost has been taken into account based on current Hp promotions at www.hp.com and assuming a laptop model with enough features for the computational load of the study.

(b): For the total cost, the unit cost of the cluster with a usage of 2 cores and 8 GB of memory in one node has been taken into account. The number of hours is assumed to be an average of 72 hours per simulation for a total of 8 simulations without taking into account the trial-and-error models.

Software Licenses

Table 7 below shows the costs of the various software licenses used during the development of the study.

Sofware License	Concept	Quantity	Unit Cost (€/u)	Total Cost (€)	Subtotal (€)
Matlab R2020b	Student License	1	69,00	69,00	
Microsoft Office 2021 Home & Student	Student License	1	149,00	149,00	
GiD simulation 16th version	Student License	1/month	60,00	300,00	518,00
Gmsh 4.9.5 version	Free License	1	0,00	0,00	
Autodesk Meshmixer	Free License	1	0,00	0,00	
ParaView 5.10.0 version	Free License	1	0,00	0,00	

Table 7. Software Licenses Costs.

Budget Summary

Cost Type	Subtotal (€)	TOTAL (€)
Human working hours	5760,00	
Material	1717,12	**7995,12**
Sofware Licenses	518,00	

Table 8. Total Costs.

REFERENCES

Bonet J. and Wood R.D. Non-linear continuum mechanics for finite element analysis. *Cambridge University Press*, 1997.

Brennan J, Norris DP, Robertson EJ. 2002. Nodal activity in the node governs left-right asymmetry. *Genes & Development* 16:2339–2344. doi: https://doi.org/10.1101/gad.1016202,

Brown, N. A. and Wolpert, L. (1990). The development of handedness in left/right asymmetry. *Development* 109, 1-9.

Buckingham M, Meilhac S, Zaffran S. Building the mammalian heart from two sources of myocardial cells. *Nat Rev Genet*. 2005 Nov; 6(11):826-35. doi: 10.1038/nrg1710.

Carro Hevia, A., Santamarta Liébanab, E., Martín Fernándeza, M. (2011). "Síndrome de heterotaxia" in *Cardiocore*, Vol. 46, Issue 2, April–June 2011, Pages e23-e26.

Chen, C. K., Kü hnlein, R. P., Eulenberg, K. G., Vincent, S., Affolter, M. and Schuh, R. (1998). The transcription factors KNIRPS and KNIRPS RELATED control cell migration and branch morphogenesis during Drosophila tracheal. *Development* 125, 4959-4968.

Davis, N. M., Kurpios, N. A., Sun, X., Gros, J., Martin, J. F. and Tabin, C. J. (2008). The chirality of gut rotation derives from left-right asymmetric changes in the architecture of the dorsal mesentery. *Dev. Cell* 15, 134-145.

Desgrange A, Le Garrec JF, Meilhac SM. Left-right asymmetry in heart development and disease: forming the right loop. *Development*. 2018 Nov 22; 145(22): dev162776. doi: 10.1242/dev.162776.

Geuzaine C., Remacle J.F., (2009) "Gmsh: A 3-D finite element mesh generator with built-in pre- and post-processing facilities" in *International Journal for numerical methods in engineering*. Volume79, Issue11 10 September 2009 Pages 1309-1331.

Guimier A, Gabriel GC, Bajolle F, Tsang M, Liu H, Noll A, Schwartz M, El Malti R, Smith LD, Klena NT, Jimenez G, Miller NA, Oufadem M, Moreau de Bellaing A, Yagi H, Saunders CJ, Baker CN, Di Filippo S, Peterson KA, Thiffault I, et al. 2015. MMP21 is mutated in human heterotaxy and is required for normal left-right asymmetry in vertebrates. *Nature Genetics* 47:1260–1263. doi: https://doi.org/10.1038/ng.3376.

Ivanovitch, K. et al. (2017) Live imaging of heart tube development in mouse reveals alternating phases of cardiac differentiation and morphogenesis. *eLife* 6, e30668.

Iwaki, D. D. and Lengyel, J. A. (2002). A Delta-Notch signaling border regulated by Engrailed/Invected repression specifies boundary cells in the Drosophila hindgut. *Mech. Dev*. 114, 71-84.

Karner, C. M., Chirumamilla, R., Aoki, S., Igarashi, P., Wallingford, J. B. and Carroll, T. J. (2009). Wnt9b signaling regulates planar cell polarity and kidney tubule morphogenesis. *Nat. Genet*. 41, 793-799.

Kennaway R, Coen E, Green A, Bangham A. Generation of diverse biological forms through combinatorial interactions between tissue polarity and growth. *PLoS Comput Biol*. 2011 Jun;7(6):e1002071. doi: 10.1371/journal.pcbi.1002071. Epub 2011 Jun 16.

Kidokoro, H., Okabe, M. and Tamura, K. (2008). Time-lapse analysis reveals local asymmetrical changes in C-looping heart tube. *Dev. Dyn*. 237, 3545-3556.

Le Garrec JF, Domínguez JN, Desgrange A, Ivanovitch KD, Raphaël E, Bangham JA, Torres M, Coen E, Mohun TJ, Meilhac SM. A predictive model of asymmetric morphogenesis from 3D reconstructions of mouse heart looping dynamics. *Elife*. 2017 Nov 28;6:e28951. doi: 10.7554/eLife.28951.

Lee B. Beerman, (2020), Children's Hospital of Pittsburgh of the University of Pittsburgh; *School of Medicine*. MD. Available on: <https://www.msdmanuals.com/es-es/professional/pediatr%C3%ADa/anomal%C3%ADas-cardiovasculares-cong%C3%A9nitas/transposici%C3%B3n-de-las-grandes-arterias-tga>

Lin AE, Krikov S, Riehle-Colarusso T, Frıᯠas JL, Belmont J, Anderka M, Geva T, Getz KD, Botto LD, National Birth Defects Prevention Study. 2014. Laterality defects in the national birth defects prevention study (1998-2007): Birth prevalence and descriptive epidemiology. *American Journal of Medical Genetics Part A* 164:2581–2591. doi: https://doi.org/10.1002/ajmg.a.36695

Mandrycky CJ, Williams NP, Batalov I, El-Nachef D, de Bakker BS, Davis J, Kim DH, DeForest CA, Zheng Y, Stevens KR, Sniadecki NJ. Engineering Heart Morphogenesis. *Trends Biotechnol*. 2020 Aug;38(8):835-845. doi: 10.1016/j.tibtech.2020.01.006. Epub 2020 Mar 5.

Männer, J. and Yelbuz, T.M. (2019) Functional morphology of the cardiac jelly in the tubular heart of vertebrate embryos. *J. Cardiovasc*. Dev. Dis. 6, 12.

Manning, A. and McLachlan, J. C. (1990). Looping of chick embryo hearts in vitro. *J. Anat*. 168, 257-263.

Mishra, S. (2015). Cardiac and non-cardiac abnormalities in heterotaxy syndrome. *Indian J. Pediatr*. 82, 1135-1146.

Oostra, R.-J. et al. (2007) Outlines of external development. In Steding's and Virágh's *Scanning Electron Microscopy*.

Sizarov, A. et al. (2011) Formation of the building plan of the human heart: morphogenesis, growth, and differentiation. *Circulation* 123, 1125–1135.

Van Vliet, P. et al. (2012) Early cardiac development: a view from stem cells to embryos. *Cardiovasc. Res*. 96, 352–362

Wang, J., Mark, S., Zhang, X., Qian, D., Yoo, S.-J., Radde-Gallwitz, K., Zhang, Y., Lin, X., Collazo, A., Wynshaw-Boris, A. et al. (2005). Regulation of polarized extension and planar cell polarity in the cochlea by the vertebrate PCP pathway. *Nat. Genet*. 37, 980-985.

ANNEXES

A.1 <u>Contact Functions</u>

- ❖ Link: <u>gKContact Function</u>
- ❖ Link: <u>SetDefaults Function</u>
- ❖ Link: <u>SetContacts Function</u>

A.2 <u>Dynamics Function</u>

- ❖ Link: <u>gkDynamics Function</u>

A.3 <u>Elasticity Functions</u>

- ❖ Link: <u>Qe4QE Function</u>
- ❖ Link: <u>MassMatrix Function</u>
- ❖ Link: <u>ke4QE Function</u>
- ❖ Link: <u>gStrNeoElem Function</u>
- ❖ Link: <u>gStrLElement Function</u>
- ❖ Link: <u>gStr Function</u>
- ❖ Link: <u>gKViscoElasticLElement Function</u>
- ❖ Link: <u>gKNeoElem Function</u>
- ❖ Link: <u>gKElastic Function</u>

A.4 <u>Friction Function</u>

- ❖ Link: <u>gkSubstrate Function</u>

A.5 <u>Geometry Functions</u>

- ❖ Link: <u>CheckShape Function</u>
- ❖ Link: <u>DefineGrowth Function</u>
- ❖ Link: <u>InitProblem Function</u>
- ❖ Link: <u>MeshGen Function</u>

A.6 <u>Input Parameters Functions</u>

- ❖ Link: Contact <u>InputParametersC Function</u>
- ❖ Link: Non-Contact <u>InputParametersNC Function</u>

A.7 <u>Post-Processing Functions</u>

- ❖ Link: OutputMatlab Function
- ❖ Link: OutputSubstrateVTK Function
- ❖ Link OutputVTK Function
- ❖ Link: WriteVTKMesh Function
- ❖ Link: WriteVTKResElemental Function
- ❖ Link: WriteVTKResNodal Function

A.8 <u>Solve Functions</u>

- ❖ Link: gK Function
- ❖ Link: Renumber Function
- ❖ Link: Solve Function
- ❖ Link: SolveViscoGrowth Function

A.9 <u>Viscogrowth (FEM)</u>

- ❖ Link: MainViscoGrowth Function

A.10 <u>Angle Twist Analysis</u>

- ❖ Link: TwistAngle Function